RADAR OBSERVATIONS OF GEOSYNCHRONOUS ORBITS

D. Mehrholz

Research Institute for High Frequency Physics (FGAN–FHP),
Neuenahrer Str. 20, 53343 Wachtberg, Germany

ABSTRACT

The paper describes ground–based radar techniques for the observation of objects in GEO. The problem of generating orbital elements of sufficient accuracy from radar data with severe limitations in the signal–to–noise ratio (S/N) is discussed. The high Doppler resolution monopulse technique can be used to discriminate objects orbiting close together in the antenna beam. For sufficient S/N ratios this technique is applicable for assessments of attitude and cross–range dimensions of observed objects.

1. INTRODUCTION

The space debris situation is of concern to the construction and operation of satellites in all orbits. The need for risk assessments and control of mitigation measures calls for appropriate models describing the debris environment and its future development. At present models must be improved to reduce uncertainties in the results and models must be verified by measurements. Since it is currently impossible to track all debris in orbit, the debris flux is sampled in selected search volumes which are observed prefereably for at least 24 hours.

A variety of ground–based radars and telescopes with optical and infrared sensors have been employed to measure objects mainly in low Earth orbits (LEO). The employment of space based sensors is limited today to the LEO–environment for assessments of the orbital population of very small debris. Observation of space objects orbiting in or near the geosynchronous Earth orbit (GEO) is mainly performed with optical telescopes. GEOs are nearly circular with any inclination having orbital periods of $\approx$ 24 hours. Operational satellites can be manoeuvered in order to keep a position at the same longitude on the Earth throughout their orbit. Inoperational satellites and space debris are orbiting above and below GEO, they are therefore not continously observable.

Since up to today only some limited effort was performed to sample GEOs with ground–based radars or electro–optical deep–space sensors, no comprehensive surveys of the geostationary ring have been conducted and the size and number of its uncataloged population remains unclear.

Ground–based radars are well suited to observe space objects due to their all–weather and day–and–night performance. However, the radar energy budget will always be a limiting factor for detection of small objects at high ranges. The only radar in Germany for space object observations is FGAN–FHP's experimental *Tracking and Imaging Radar (TIRA)* system. With single impulses of the L–band tracking radar objects of 2 cm size are detectable at 1000 km range. Using coherent multi–impulse integration 1 m sized objects can be measured in GEO. The detection of 30–40 cm objects in GEO seems to be possible.

Section 2 of this paper gives a short overview on cataloged objects in GEO. In section 3 the scenery for observations of drifting objects in GEO is described. The radar detection performance in general and with respect to the TIRA system is highlighted in section 4. This section also contains discussions on how accurate geosynchronous orbits can be estimated from radar measurements, how to discriminate objects being simultaneously illuminated by the radar beam, and what additional information can be gained from narrowband radar measurements.

2. OVERVIEW ON CATALOGED OBJECTS

U.S. SPACE COMMAND tracks and catalogs Earth orbiting active spacecraft and space debris employing their worldwide Space Surveillance Net of radar and optical sensors. The NASA–Catalog, which is the basic source for ESA/ESOC's DISCOS Database, contains at present a total of 8191 unclassified objects characterized as:

Table 1. Cataloged objects, 07.03.1997, (Ref. 1).

Payloads	2.117
Rocket bodies	1.353
Debris	4.653
Unknown	68
Total	8.191

Assessments reveal, that only 5–6% are operational satellites. A snapshot of the distribution of nearly all currently orbiting objects is shown in Fig. 1 (computed from NASA Two–Line–Elements, TLE). The left–hand part views towards the North Pole whereas the right–hand part views into the equator plane.

Proceedings of the Second European Conference on Space Debris, ESOC, Darmstadt, Germany, 17-19 March 1997, (ESA SP-393, May 1997)

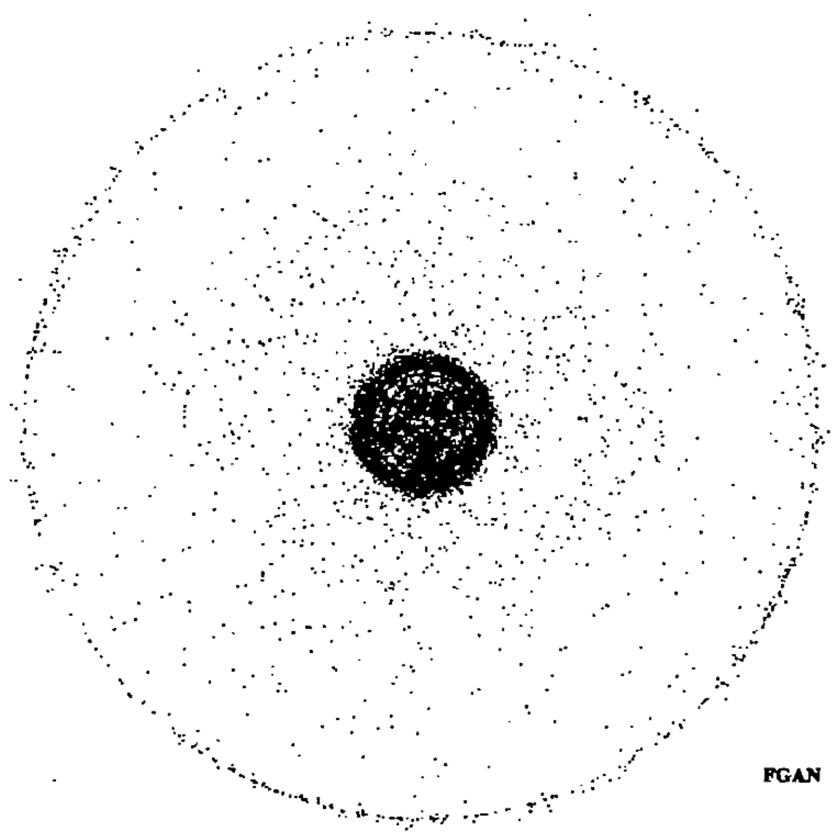

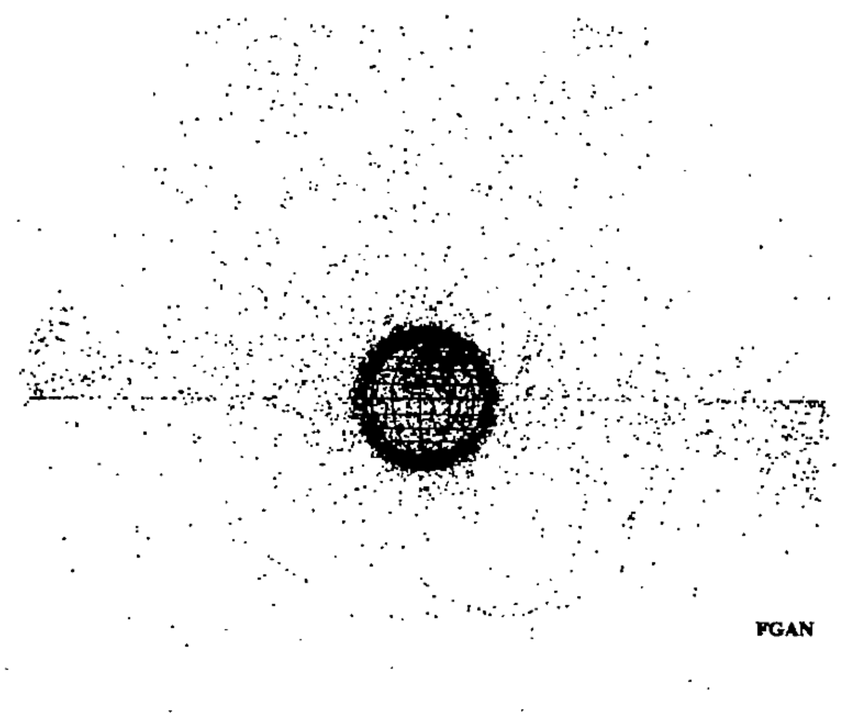

Figure 1. Snapshot of cataloged objects on Earth orbits.

High concentration of objects in LEO, different distributions in northern and southern hemisphere due to highly excentrical orbits, and the populations in GEO and GTO (geostationary transfer orbits) become visible.

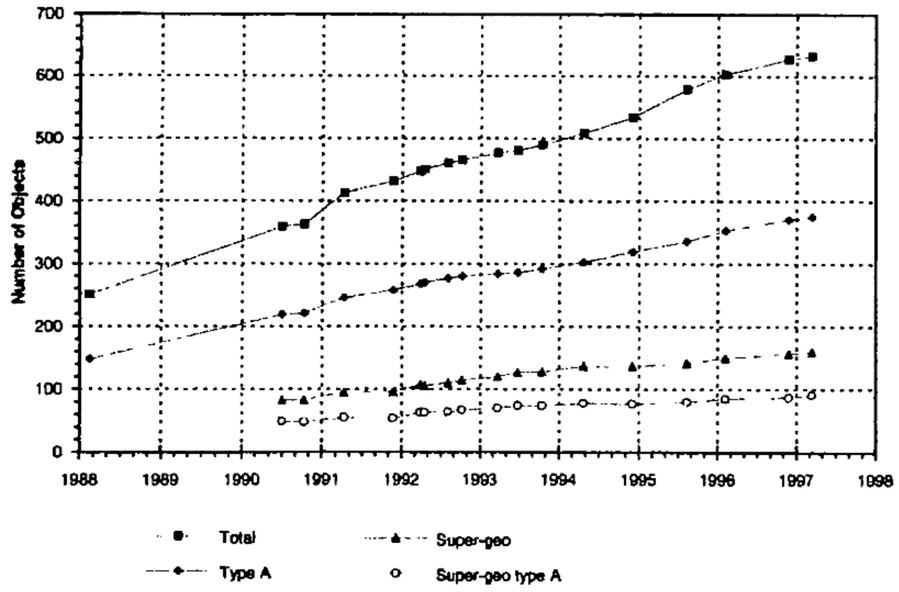

Figure 2. Object count for GEO and Super-GEO.

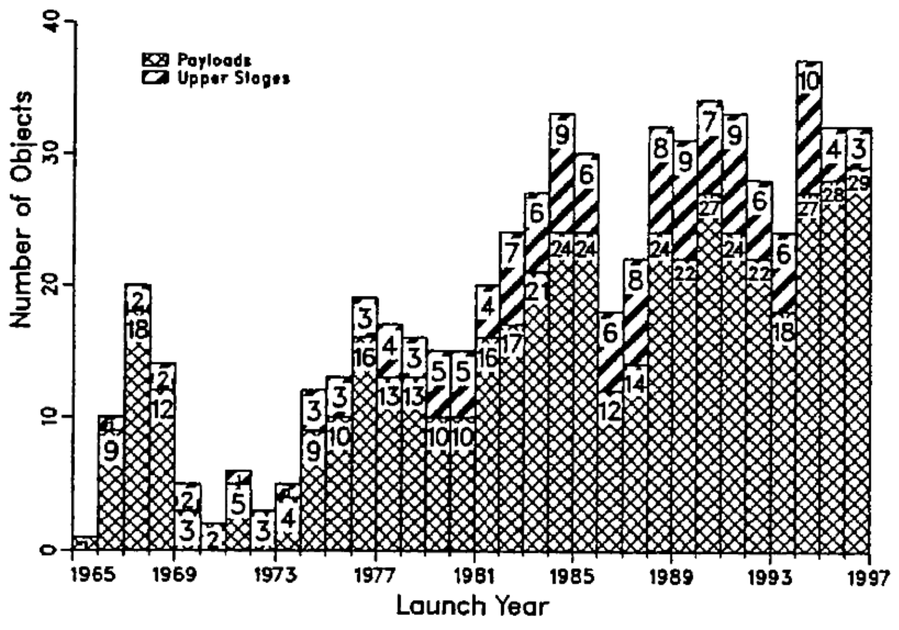

Figure 3. Yearly number of objects launched in GEO.

The minimum sizes of objects in the NASA–Catalog are 10–20 cm in LEO and about 1 m in GEO. Based on this catalog ESA/ESOC produces with their DISCOS Database frequently a log of objects near the geostationary ring. According to this log there were 632 objects cataloged on geostationary and near–geostationary orbits by March 1997. Fig. 2 shows the increase of objects and type A (main payloads) objects count in GEO from February 1988 till March 1997. Fig. 3 gives the yearly number of payloads and upper stages launched into GEO (Ref. 2).

At present the most significant force of removing debris from low altitude orbits is atmospheric drag. At greater altitudes like GEO, moving a satellite into a higher orbit has become international standard practice. However, space debris generated in GEO will stay in orbit for million of years since there are no natural sinks and removal by retrieval is not feasible with todays technology.

3. SCENERY FOR OBSERVATIONS IN GEO

3.1 Background

Space objects not being exactly in geosynchronous orbits are drifting relative to a position at the same longitude on the Earth. The drift velocity ω_λ (drift in direction of the geographical longitude λ) can be assessed, knowing object's mean motion n:

$$\omega_\lambda = (1.00274 - n) \cdot 360^o \qquad \text{in degree/day} \qquad (1)$$

Fig. 4 shows a set of TLE for the non–operational satellite TVSAT–1 (Object No.: 18570, international launch designation: 87 095 a):

```
1 18570U 87095a 94155.84957839 -.00000292 00000+0 10000-3
2 18570 4.7877 62.5377 0013658 292.5816 353.7081 0.99143361
```

Figure 4. TLE for TVSAT–1.

Taking for example the mean motion $n = 0.99143361$ from the above TLE one computes with Eq. 1 for TVSAT–1 a drift velocity of $\omega_\lambda = 4.07^o$/day.

Table 2. Examples for the observability of some satellites in GEO, computed for FGAN's TIRA Station, $\varphi_{TIRA} = 50.6174^o$.

Satellite		n	a	Drift	Window		Period
No.	ID	1/d	km	$\omega_\lambda/^o$/d	$\Delta_{OW,\lambda}/^o$	$\Delta_{OW,d}$/d	$T_{OW,\lambda}$/d
18570	TV1	0.99143361	42484	4.070	152.7	37.5	88.5
19017	G15	0.97826178	42865	8.812	152.9	17.4	40.9
20122	OL1	1.01366330	41861	-3.932	152.2	38.7	91.6
11841	GO4	0.98629274	42632	5.921	152.8	25.8	60.8
17083	GO13	0.96724677	43189	12.778	153.1	12.0	28.2
21533	GO23	0.98909809	42551	4.911	152.7	31.1	73.3

Drifting satellites are only periodically observable. Let the width of observation windows (OW) in longitudinal direction be $\Delta_{OW,\lambda}$ in degree or $\Delta_{OW,d}$ in days, and the period of periodical observations $T_{OW,d}$ in days. The observability can then be assessed with Eqs. 2 - 4 assuming $i = e = 0$ and a spherical Earth:

$$\Delta_{OW,\lambda} \approx 2 \cdot \arccos\left(\frac{R_E}{a} \cdot \frac{1}{\cos\varphi_B}\right) \quad (2)$$

$$\Delta_{OW,d} = \frac{\Delta_{OW,\lambda}}{|\omega_\lambda|} \quad (3)$$

$$T_{OW,d} = \frac{360^o}{|\omega_\lambda|} = \frac{1}{|1.00274 - n|} \quad (4)$$

with

$$a^3 = \frac{\mu}{4 \cdot \pi^2 \cdot n^2} \quad , \quad \omega_\lambda = \frac{1}{1.00274 - n} \quad (5)$$

and $R_E = 6371$ km (radius of the spherical Earth), $\mu = 398600.5$ km^3/s^2, a: geocentrical radius of the orbit, φ_B: geographical latitude of the observation station.

Table 2 shows drift velocities ω_λ, width of observation windows $\Delta_{OW,\lambda}$, $\Delta_{OW,d}$ as well as length of observation periods $T_{OW,\lambda}$ for some non–operational satellites in GEO, computed for FGAN's TIRA station.

3.2 Representation of observation windows

For planing observation campaigns of drifting objects in GEO and for adaptation of the radar signal processing to the special situation, where targets are in ambigious range (that means the signal round–trip–time is larger than the radar pulse repetition period $T_p = 1/f_{PRF}$) and the radar echoes are buried in noise (so that multi–impulse integration of succeeding echoes becomes necessary) a typical case is studied.

Fig. 5 presents an observation window for TVSAT–1 computed from a set of TLE of epoche 94–195.76 for the TIRA station. The time period spans 45 days, the length of the observation window was assessed to be $\approx$ 37.5 days (see Table 2). Shown are the observation vector components azimuth az, elevation el, range r, and range rate $\dot{r}$ as functions of time. The length of the short periodicals in the plots is typically $T_p = 1/n$, its amplitude depends on the orbit inclination i which is for TVSAT–1 $i = 4.7877^o$.

The range of changes of the aspect angles elevation and azimuth ($el = f(az)$) as well as for range rate and range ($\dot{r} = g(r)$) are shown in Fig. 6 for a selected day. The parameter in both plots is daytime in hours. The azimuth drift is about 4.7^o (corresponding well with the assessed longitudinal drift velocity ω_λ, see Table 2, taking an average elevation of about 30^o into account). The aspect angle in elevation varies in 24 hours by about 9.4^o. Variation in range is about 740 km. The changes in range rate are in the range of -28 m/s $\leq \dot{r} \leq$ 32 m/s in 24 hours. Information contained in Fig. 6 are essential for assessments of the optimal length of coherent multi–impulse integration intervals.

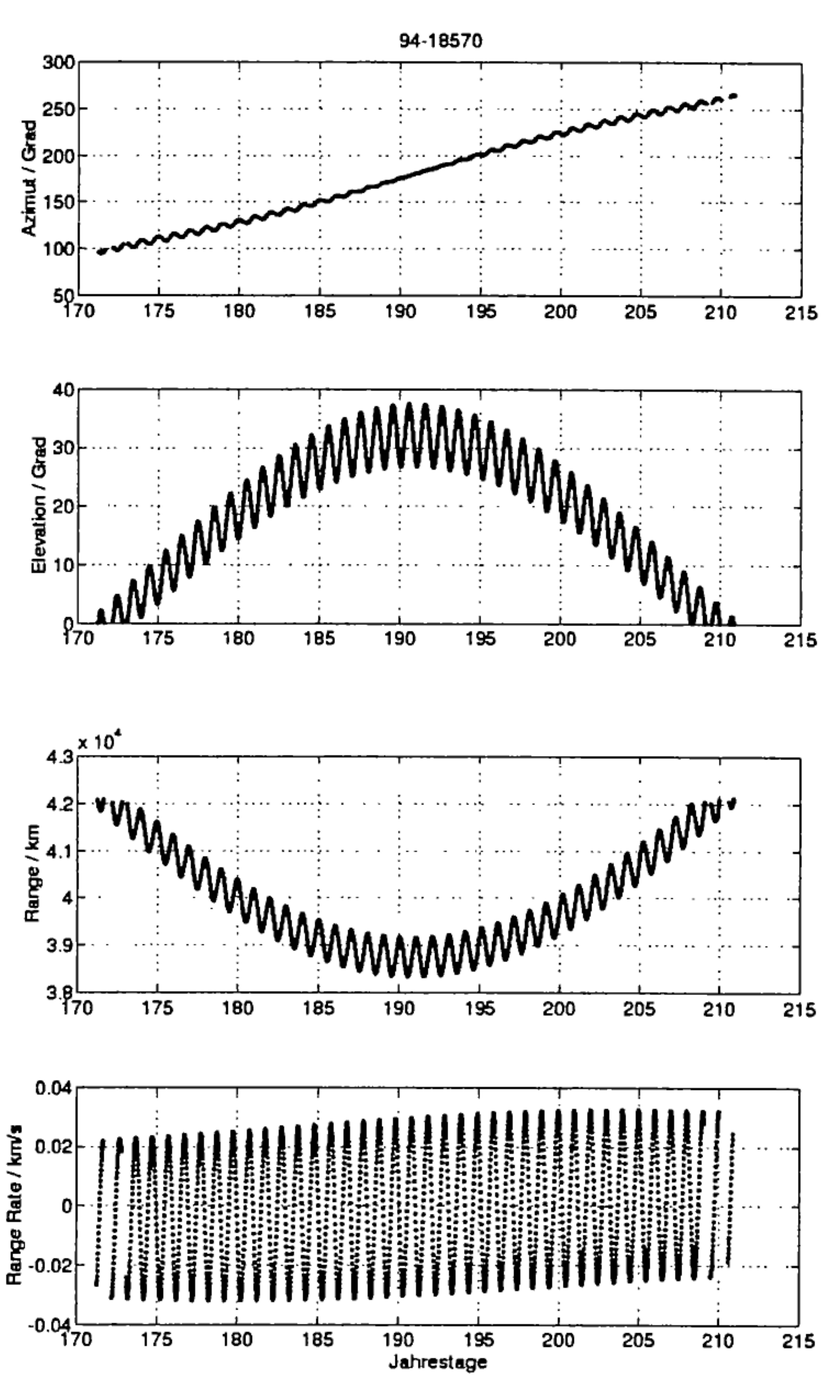

Figure 5. Observation window for TVSAT–1 of about 37.5 days, 20.06.1994 – 29.07.1994, 20 minutes time steps, computed from TLE 94–195.76 for the TIRA station.

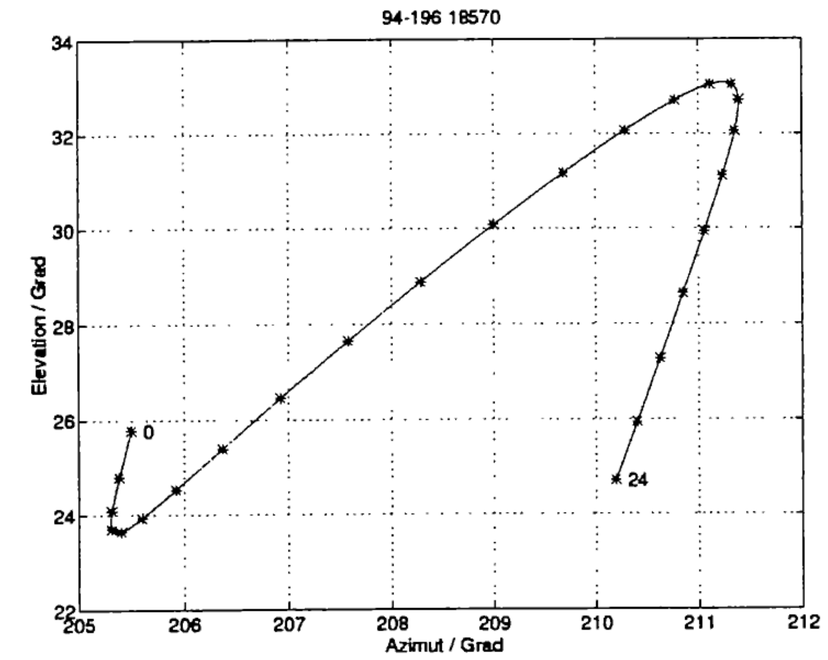

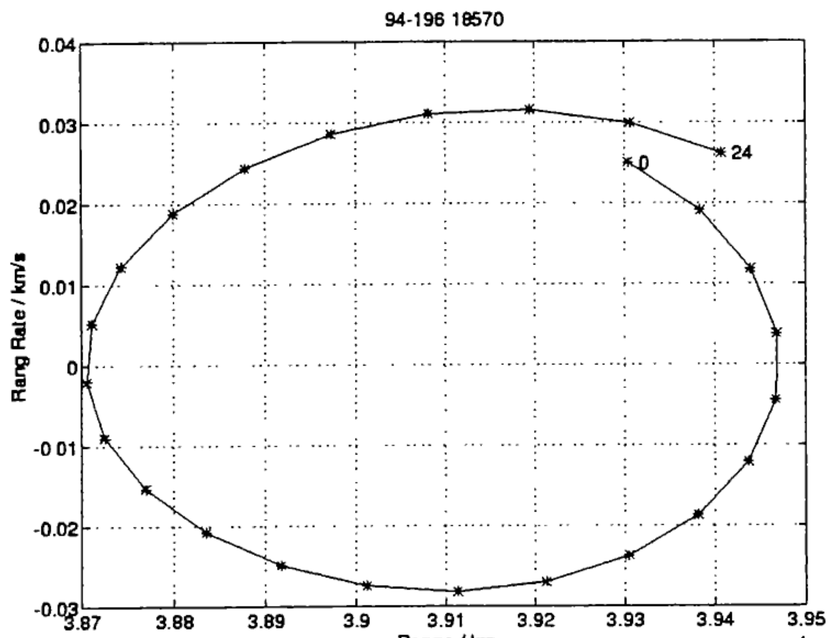

Figure 6. Range of changes in azimuth, elevation, range, and range rate for TVSAT–1 for 15.07.1994. The parameter in the plots is daytime in hours. Plots are computed from TLE 94–195.76 for the TIRA station.

4. RADAR MEASUREMENTS IN GEO

For radar observations of objects in or near to the geostationary ring one is faced with the following questions:

- How to solve the radar energy budget for observation of small objects at high ranges?
- What are the sizes of the smallest detectable and measurable objects in GEO?
- How accurate can geosynchronous orbits be estimated from radar measurements?
- Can the signal processing discriminate between targets being simultaneously illuminated by the radar beam? (A 0.5^o field–of–view is about 370 km at 42000 km range).
- What additional information can be gained from radar measurements?

In the following sections these questions will be answered with respect to the TIRA system. Examples of radar measurements and analysis results will be discussed.

4.1 Radar detection performance

The reason for the existence of a minimum detectable signal level is the presence of noise. Noise is received via the antenna beam, generated in the receiver circuits and by the radar transmitter. With $N_o = kT_s = kT_oF_n$ for the spectral density of the noise power (per unit bandwidth) and $B_n = 1/\tau$ for the noise bandwidth (τ radar pulselength) one gets for the minimum detectable echo signal power $P_{r,min}$ and for the maximum detection range R_{max}:

$$P_{r,min} = (S/N)_{min} kT_o F_n B_n \tag{6}$$

$$R_{max} = \left[\frac{P_t \tau G_t G_r \sigma \lambda^2}{(4\pi)^3 (S/N)_{min} kT_o F_n L} \right]^{1/4} \tag{7}$$

with $k = 1.38 \cdot 10^{-23}$ Ws/^{o}K (Boltzmann figure), T_s system noise temperature, $T_o = 290^oK$, F_n system noise figure, P_t transmitted peak power, G antenna gain, σ Radar–Cross–Section (RCS), λ radar wavelength, L losses.

Fig. 7 shows for FGAN's L–band tracking radar of the TIRA system the detection range (R in km) as function of the target RCS (in dB square meter) for single pulse processing (see also Fig. 8). The corresponding radar parameters are noted.

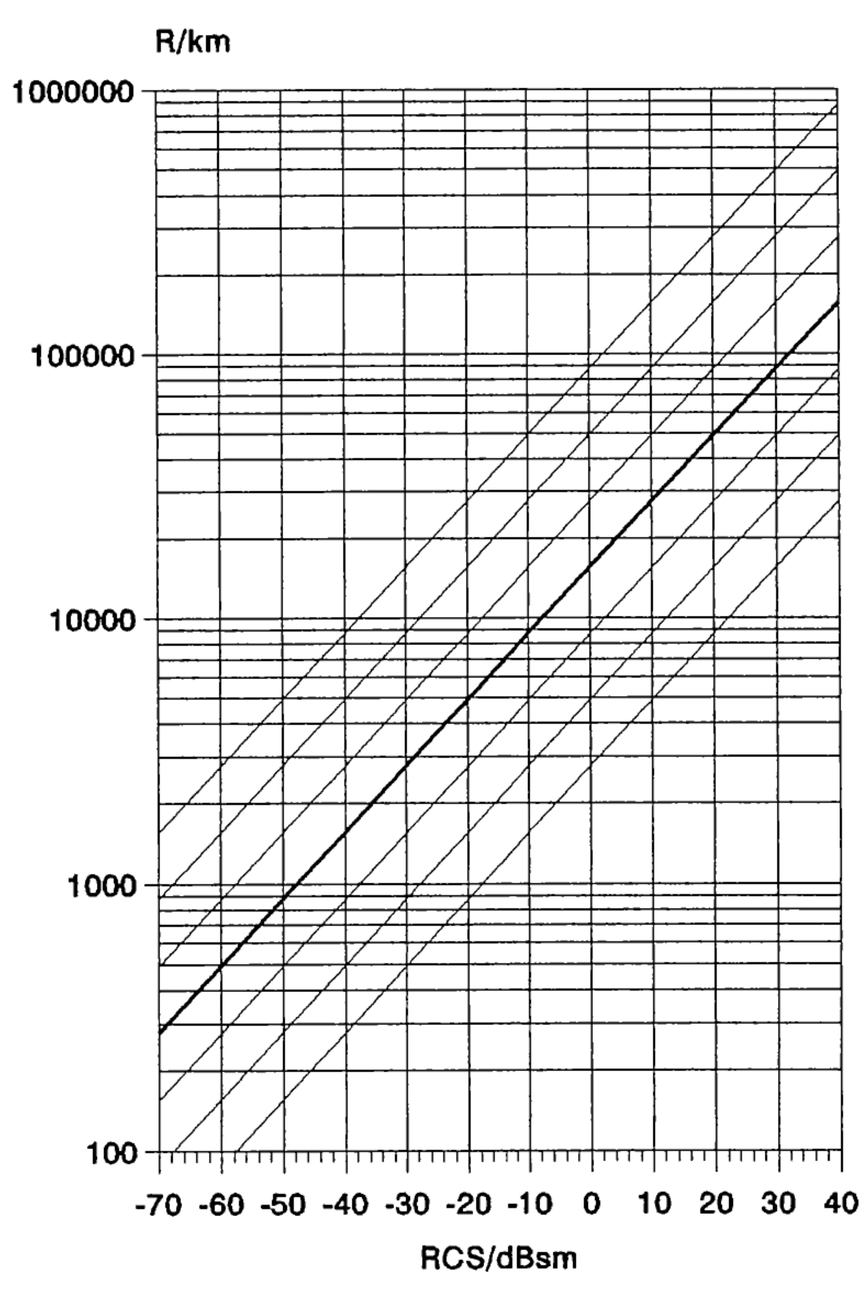

Figure 7. Radar detection performance for single pulse processing of TIRA's L–band tracking radar for: Peak power $P = 1.6$ MW, pulse length $\tau = 1$ ms, and elevation angle $\geq 60^o$. The bold solid line holds for a S/N ratio of 0 dB. The other lines are for: -30 dB $\leq S/N \leq 30$ dB in 10-dB-steps.

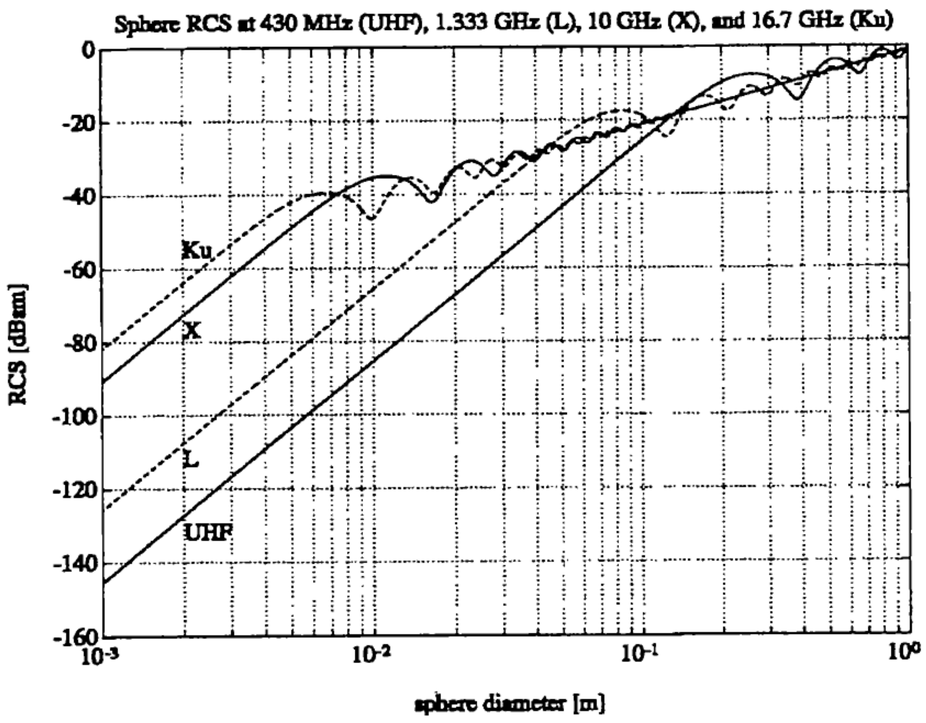

Figure 8. RCS in dBsm for perfectly conducting spheres for different radar carrier frequencies.

Data presented in Fig. 7 result from analysis of the COBEAM–1/96 experiment (Cooperative Beam–Park Measurements, Refs. 3, 4) and from the NASA ODERACS '94/95 experiments (Orbital Debris Radar Calibration Spheres), where the TIRA system tracked 5 cm metalic spheres frequently at 2200 km maximum range. It is assumed, that with coherent multi–impulse processing techniques 1 m objects can be measured in GEO (with S/N$\geq$10 dB). The detection of 30–40 cm objects (with S/N$\approx$3 dB) in GEO should be possible.

Fig. 8 shows the RCS in dBsm for perfectly conducting spheres of diameter $d = 2r$ for different radar carrier frequencies f. With wavelength λ:

$$\lambda = c/f \tag{8}$$

(c velocity of light) three distinct regions might be recognized. It is common practice to define these regions by the number $kr = 2\pi r/\lambda$:

$$\begin{aligned} kr &< 1: \text{ Low–frequency– or Raleigh–region} \\ 1 \leq kr &< 10: \text{ Resonance– or Mie–region} \\ 10 &\leq kr: \text{ High–frequency– or optical–region} \end{aligned}$$

It is found that the RCS of objects in the Raleigh–region follows the relation $\sigma \sim \lambda^{-4}$ and is not a function of the details of the object (tendency to volume scattering). RCS assessments of objects in the Mie–region (object dimensions in the range of radar wavelength) are the most difficult ones. The fundamental problem of estimating e.g. the space debris size from RCS measurements in this region becomes evident: For a given RCS of a sphere one can select up to three corresponding sphere diameters. However, this ambiguity problem can be solved by using simultaneously two different radar carrier frequencies, e.g. L–band and Ku–band (which is possible with the TIRA system). In the high–frequency–region, where the object dimensions are large compared to the wavelength, surface and edge scattering effects play the dominate role. The proportionality of the RCS may range from a λ^{-2} to a λ^{2} law, depending on the type and strength of surface curvature.

4.2 TIRA's three subsystems

TIRA is an experimental system developed to assist radar research. The system consists mainly of three subsystems:

- The 34–m parabolic antenna:
  The 34–m parabolic antenna is a fully computer controlled elevation–over–azimuth pedestal. The maximum velocity is 24°/s in azimuth and 6°/s in elevation. The resolution of the angular position encoders is 20 bit corresponding to 1.24". The system is protected by a radom of 49 m diameter (Fig. 9).

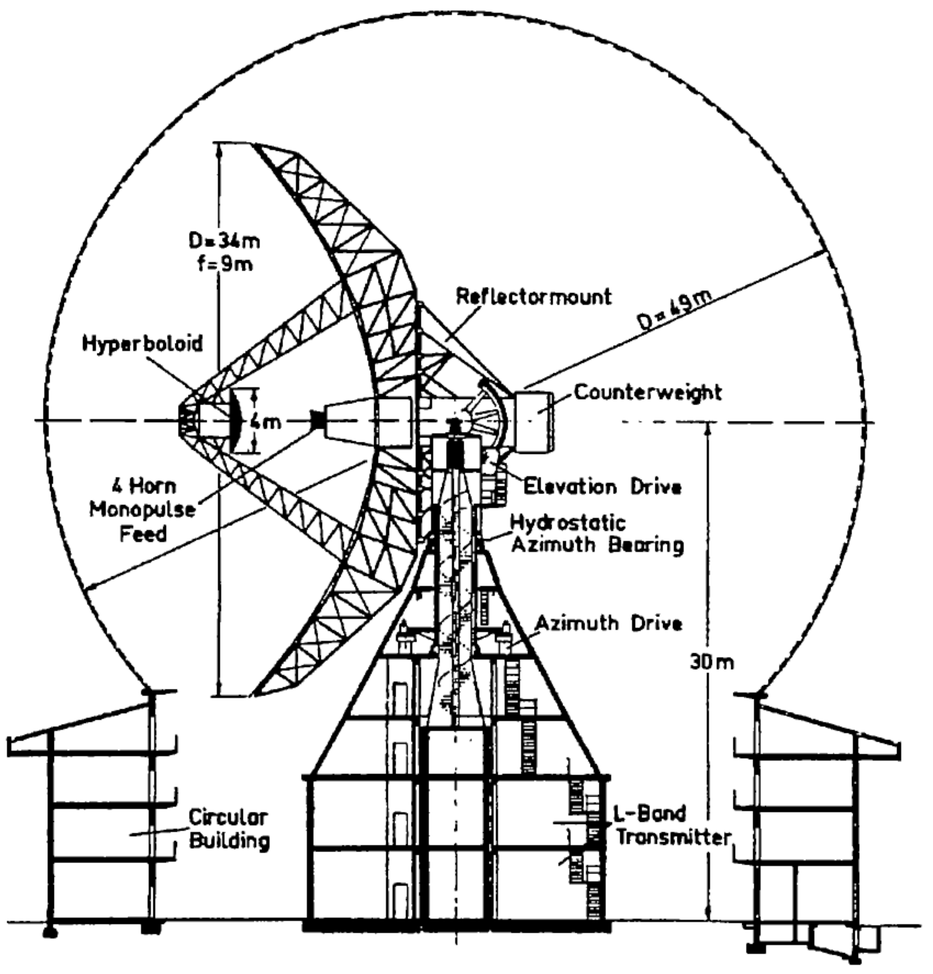

Figure 9. 34–m parabolic antenna of the TIRA system at FGAN, Wachtberg, Germany.

- The L–band monopulse tracking radar:
  The L–band monopulse tracking radar is a coherent narrowband radar using pulse compression to improve the range resolution (at present the highest resolution is 600 m). The signal processing realizes quadrature–correlators in the tracking loops. At a pulse length of 1 ms raw radar data for the computation of about 30 observation vectors per second can be gained (4% duty cycle of the high power amplifier stage). The main vector components are: Time, azimuth, elevation, range, range rate, echo amplitude and phase, transmitted peak power and other radar parameters.
- The Ku–band imaging radar:
  The Ku–band imaging radar is a coherent high range resolution radar using linearly frequency modulated impulses of at present up to 800 MHz bandwidth (corresponding to 25 cm range resolution employing Hamming windows). The signal processing gains up to 400 data vectors per second. Each data vector contains a deramped quadrature demodulated and digitized echo signal (8 bit, 2*1024 samples), transmitted peak power and other radar parameters.

4.3 L–band measurements of GEO objects

In general the radar echoes of GEO objects are buried in noise. Fig. 10 shows the echo amplitude as function of time measured with the TIRA L–band tracking radar during the observation of TVSAT–1 in 1994.

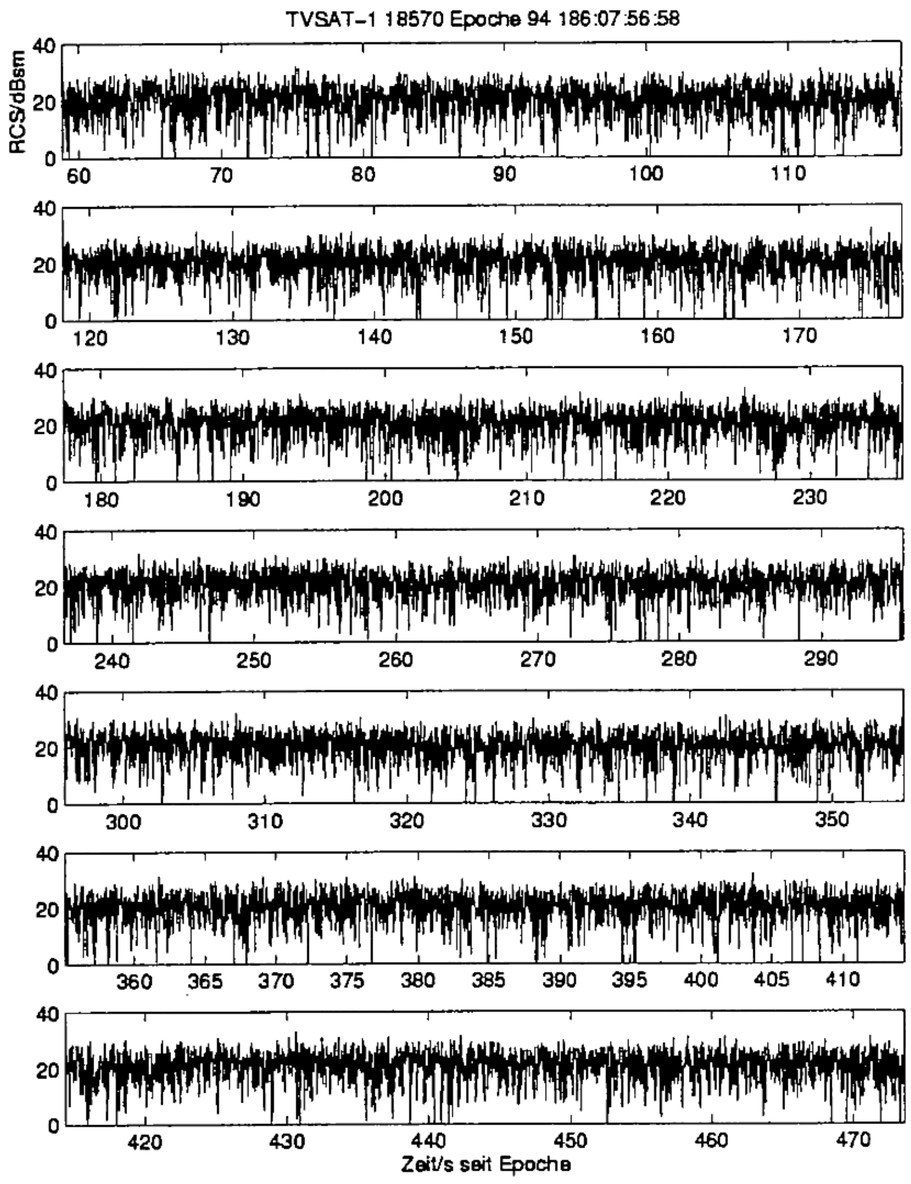

Figure 10. Echo amplitude as function of time (in seconds) measured with the TIRA L–band tracking radar (sum–channel of the 4–horn monopulse feed) during the observation of TVSAT–1 at 1994–186:07:56:58.

In order to solve the S/N ratio problem a multiple–impulse processing technique is adopted. In using this technique a sufficient number of successive echoes has to be coherently integrated. An increase of the S/N ratio due to coherent integration can only be expected if there is:

- Only very little target fluctuation,
- a predictable phase behaviour, and
- only little variation of the range rate

in the integration interval. If these requirements are not met, coherent integration will yield no processing gain at all or might even lead to a complete loss of detection. In the coherent case, the N signal phasors are added nose to tail so that the resultant amplitude is N times the amplitude of each component, thus increasing the signal power by N^2. Since system noise (assumed gaussian, uncorrelated) has random amplitude and phase, its phasors addition leads to an increase in average noise power level by factor N. Therefore, the overall processing gain is given by the number N of integrated impulses.

4.4 High Doppler resolution monopulse

Coherent integration provides an increase in S/N ratio rather than reducing the noise variation. It thus solely depends on the behaviour of the signal or with other words on the variation of the object Doppler frequency in the integration intervals.

In the following expressions are developed for coherent integration intervals to gain observation vectors ($T_{c,OV}$) on the one hand and cross–range resolution ($T_{c,CR}$) on the other. For the first case it should be recalled that observation vectors are describing the motion of object's center of mass. Therefore, the signal processing is not allowed to resolve the observed object in space (angles azimuth and elevation), time (range) and frequency (range rate, attitude). For objects in GEO the only critical part to be considered – in case of a narrowband radar – is the Doppler frequency behaviour: The signal spectrum has to stay in one Doppler frequency resolution cell in the interval $T_{c,OV}$. The second case is considered when the S/N ratio gained for the first case is sufficiently high. Here the basic requirement is that every scatter centre of the observed object stays in its Doppler frequency resolution cell in the interval $T_{c,CR}$.

The above mentioned Doppler frequency resolution δf_D of an object observed for the time interval T_c during which the echoes (received at pulse repetition frequency $f_{PRF} = 1/T_p$, T_p pulse repetition period) are coherently integrated, is defined in Eq. 9:

$$\delta f_D = \frac{1}{T_c} = \frac{1}{N \cdot T_p}. \tag{9}$$

The total Doppler frequency $f_D(t)$ of an observed space object is the superposition of the Doppler frequencies from the orbit motion $f_{D,o}(t)$ and of the intrinsic motion or attitude $f_{D,a}(t)$:

$$f_D(t) = f_{D,o}(t) + f_{D,a}(t). \tag{10}$$

In order to ease the discussion a simple object model is considered. It consists of only two scatter centres at distance d (like a dumb–bell) rotating with constant frequency f_a about its centre of mass and the vector of rotation is perpendicular to the radar–line–of–sight (RLOS). An assessment for the total Doppler frequency gives Eq. 11:

$$\begin{aligned} f_D(t) &= a_0 + a_1 \cdot t + a_2 \cdot t^2 + \ \ldots \\ &\quad \pm 2\pi \frac{d}{\lambda} f_a \cos(2\pi f_a t + \varphi). \end{aligned} \tag{11}$$

The first part of Eq. 11 is an approximation of the Doppler frequency due to the orbit motion. The second part is a periodical modulation of the Doppler frequency due to the assumed simple rotation. For objects in or near the geostationary ring the coefficient a_1 in Eq. 11 usually is small (see Fig. 6, for TVSAT–1 the change of range rate in one hour is $|\Delta\dot{r}| \leq 10$ m/s/h). The higher coefficients a_2, a_3 etc of the Taylor series can be neglected in many cases.

For the highest Doppler frequency spread Δf_D in an time interval $t \pm T_c/2$ with $T_c < 1/(2f_a)$ and $\varphi = 0$ follows for the time of highest Doppler frequency

change due to object rotation ($|\sin(2\pi f_a t)| = 1$) from Eq. 11:

$$\Delta f_D = a_1 T_c \mp 2\pi \frac{d}{\lambda} f_a \sin(\pi f_a T_c) \qquad (12)$$

For the estimation of observation vectors the maximum Doppler frequency spread $\Delta f_{Dmax,OV}$ of the observed object is derived from Eq. 12 with the assumption, that the total signal spectrum has to stay inside one resolution cell for the coherent integration interval $T_{c,OV}$:

$$\Delta f_{Dmax,OV} = |a_1| T_{c,OV} + 4\pi \frac{d}{\lambda} f_a. \qquad (13)$$

For cross–range resolution of the observed object the maximum Doppler frequency spread $\Delta f_{Dmax,CR}$ is derived from Eq. 12 with the assumption, that no scatter centre must leave its resolution cell for the coherent integration interval $T_{c,CR}$:

$$\Delta f_{Dmax,CR} = |a_1| T_{c,CR} + 4\pi \frac{d}{\lambda} f_a \sin(\pi f_a T_{c,CR}). \qquad (14)$$

With the requirement $\delta f_D \geq \Delta f_{Dmax,OV}$ an expression can now be developed for an optimum coherent integration interval $T_{c,OV}$ of successive echoes to be coherently integrated in order to gain observation vectors of maximum S/N ratios.

$$\frac{1}{T_{c,OV}} \geq |a_1| T_{c,OV} + 4\pi \frac{d}{\lambda} f_a. \qquad (15)$$

An assessment for the coherent integration interval $T_{c,CR}$ in order to resolve the observed object in cross–range is derived with the requirement $\delta f_D \geq \Delta f_{Dmax,CR}$.

$$\frac{1}{T_{c,CR}} \geq |a_1| T_{c,CR} + 4\pi \frac{d}{\lambda} f_a \sin(\pi f_a T_{c,CR}). \qquad (16)$$

Numerical evaluation of Eqs. 15 - 16 for the following parameters: $d = 10$ m, $T_a = 1/f_a = 350$ s, $|a_1| = 0.0025\ 1/s^2$, and $T_p = 27$ ms results in:

$$\begin{array}{lllll} T_{c,OV} & = & 0.62 \text{ s}, & N_{c,OV} & = & 23 \\ T_{c,CR} & = & 7.74 \text{ s}, & N_{c,CR} & = & 287 \end{array}$$

4.5 Generation of observation vectors

Multiple–impulse processing is demonstrated using narrowband radar measurements of the drifting TVSAT–1. Each line in Fig. 11 contains $N = 100$ echo signals of the sum–channel of TIRA's L–band monopulse feed and represents echo data of a 2.7 s time period. The echoes are buried in noise. Coherent integration of 100 echoes with FFT improves the S/N ratio by a factor of 100. Fig. 12 shows the signal spectrum. The frequency resolution is here $\delta f_D = 1/2.7$ Hz or with the general relation between Doppler frequency f_D and range rate $\dot{r}$:

$$\dot{r} = -\frac{\lambda f_D}{2} \qquad (17)$$

one gets $|\delta \dot{r}| = 41.7$ mm/s range rate.

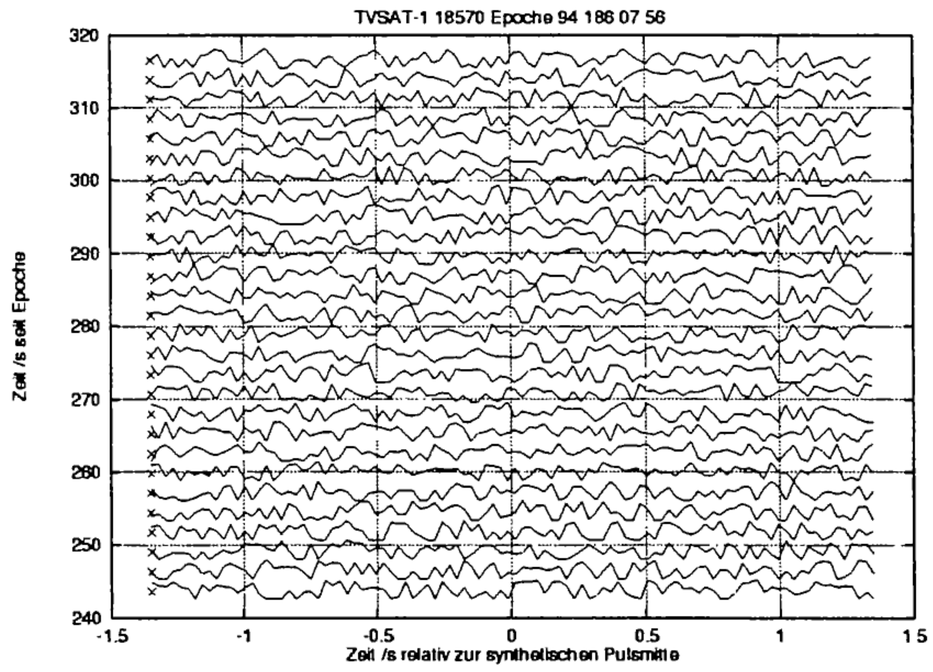

Figure 11. L–band echo amplitude (sum–channel) of TVSAT–1, measured 1994:186:07:56, $T_p = 27$ ms.

The target spectrum in Fig. 12 is close to the Doppler–zero–line. There is a slight drift due to orbit motion recognizable. The other line in this spectrum is not changing in time, it is a radar–system–line generated from the radar signal processing.

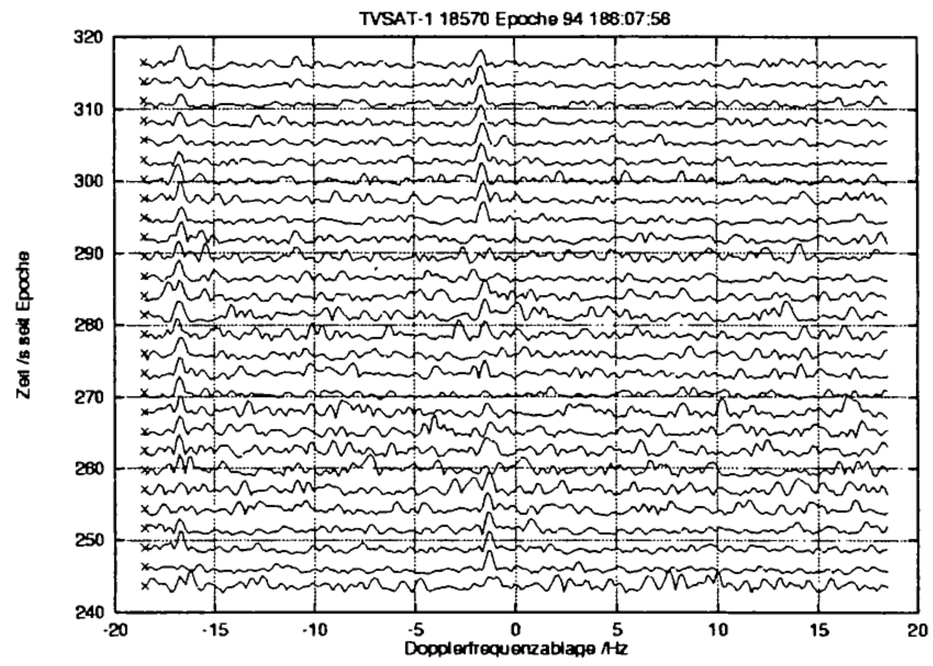

Figure 12. Signal spectrum computed with FFT, $N = 100$ from data shown in Fig. 12.

For a time interval of about 9 minutes Fig. 13 presents the signal spectrum, computed with coherent integration of 512 echoes (Ref. 5). TVSAT-1 is slightly resolved in cross–range.

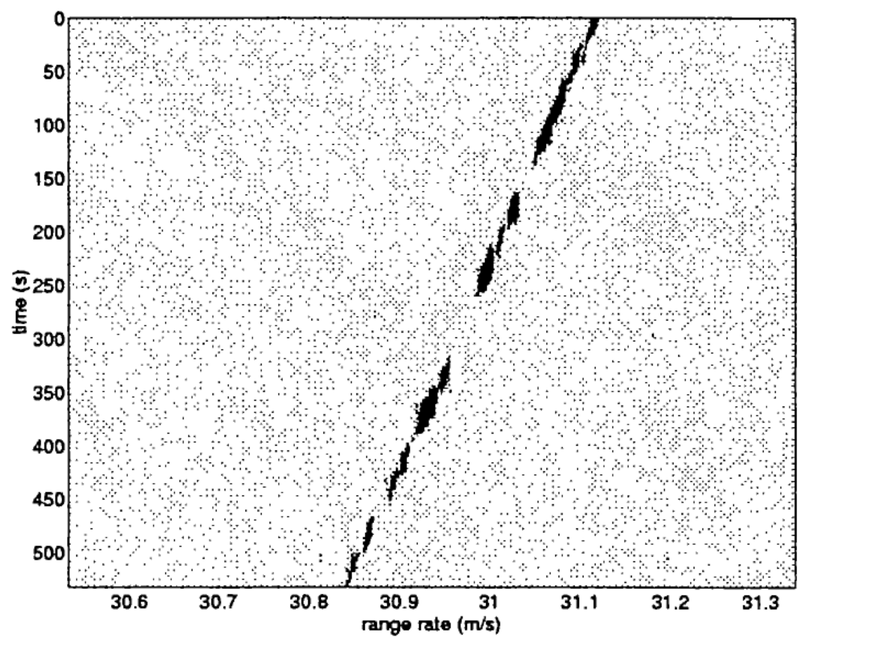

Figure 13. Signal spectrum of TVSAT-1 (see Fig. 10), measured 1994-186:07:56:58 at 156.3° azimuth, 30.0° elevation, 38,936 km range. Coherent integration of 512 single echoes providing 8.1 mm/s range rate resolution, $T_p = 27$ ms.

The effect of orbit motion becomes visible. Larger coherent integration intervals would result in further reduction of the S/N ratio. Fig. 13 could also be used to assess objects attitude. Analysis of longer observation campaigns revealed that TVSAT–1 has a rotation period of 360 s.

Doppler frequency gained as discussed from spectral analysis of raw radar data in the L–band sum–channel is used to analyse the measurements of the angular tracking channels (ΔEL and ΔTR) in elevation and transverse as well as in range thus being able to generate observation vector components and to discriminate between different objects in the radar beam. Fig. 14 shows results for TVSAT-1. A threshold of $S/N = 16$ dB was set for the generation of observation vector components.

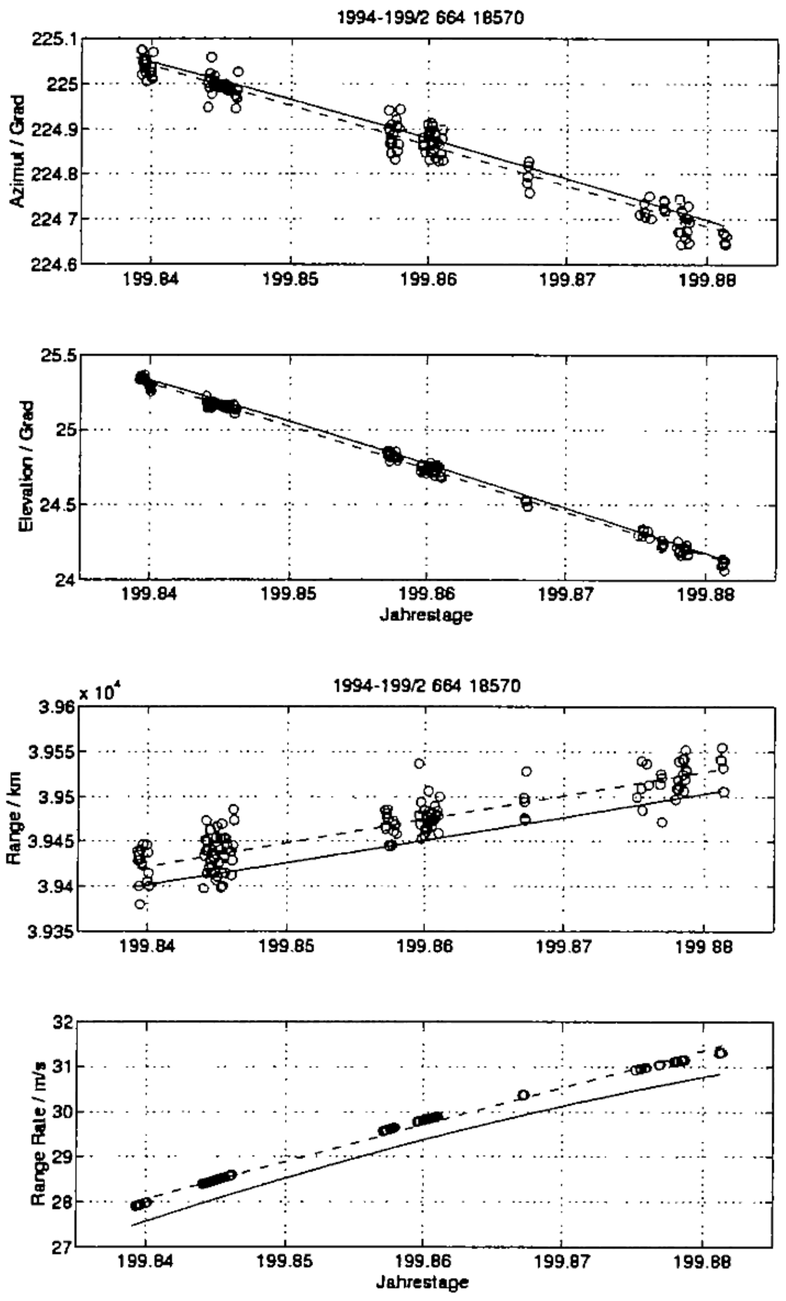

Figure 14. Observation vector components for TVSAT-1, computed from radar data measured 1994-199:20:03:56, time interval 66.37 min, S/N ratio > 16 dB, number of vectors 138.
Solid line: Vector components computed from TLE, epoch 94-195.76.
Dashed line: Best fit of vector components computed from radar data.

Results of statistical analysis of the differences between the best fit and the radar measurements are shown in Fig. 15. The standard deviations of these data were: 0.023° in azimuth, 0.022° in elevation, 18.7 km in range, and 1.9 mm/s in range rate. In general these results were confirmed by a more detailed analysis of radar and optical observations of several GEO objects (Ref. 6). For optical observations the old Zimmerwald telescope (Astronomical Institute of the University of Bern, AIUB, Switzerland) was employed.

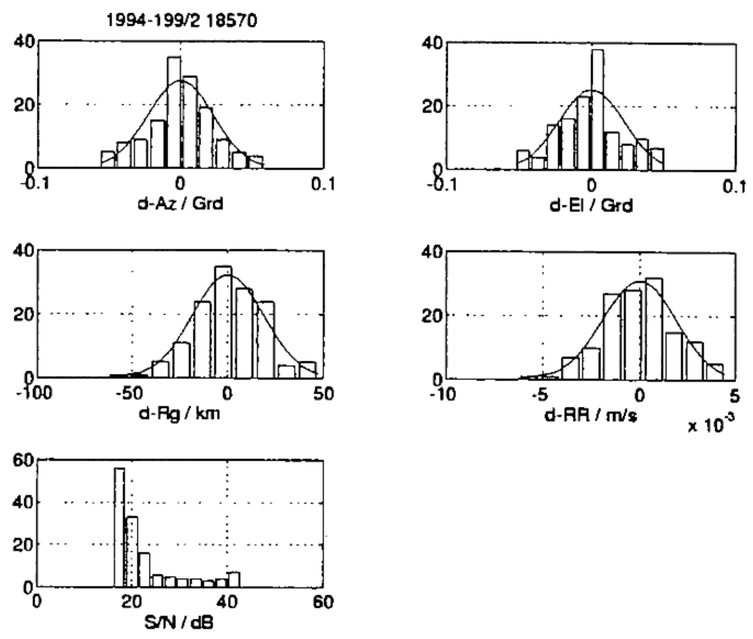

Figure 15. Standard deviations of observation vector components for TVSAT-1, computed from radar data measured 1994-199:20:03:56 (see Fig. 14) and S/N ratio histogram with 16 dB threshold. Number of analysed vectors: 138.

5. ACKNOWLEDGEMENTS

The author is indebted to the TIRA–Team of his Division "Radar Techniques for Space Reconnaissance" having designed and realized hardware and software for the TIRA system and for conducting frequently measurements and analysis of raw radar data of selected space objects.

6. REFERENCES

1. DISCOS Monthly Newsletter, *ESA/ESOC, MOD-MAS, Issue 9*, ESA/ESOC, Darmstadt, February 1997.

2. Janin, G., Log of objects near the geostationary ring, *ESA/ESOC, MOD-MAS, Issue 17*, ESA/ESOC, Darmstadt, March 1997.

3. Leushacke, L. and Jehn, R., MPIfR/FGAN cooperative beam–park experiment COBEAM–1/96, *Proceedings of IADC–13*, ESA/ESOC, Darmstadt 1996.

4. Leushacke, L., Mehrholz, D. and Jehn, R., First FGAN/MPIfR cooperative debris observation campaign: Experiment outline and first results, *Proceedings of the 2nd European Conference on Space Debris*, ESA/ESOC, Darmstadt 1997.

5. Leushacke, L., Radar Observations of GEO Objects, *Proceedings of IADC–12*, NASA, Houston, March 1995.

6. Mehrholz, D., Leushacke, L., Uschkerat, U., Schildknecht, T., and Hugentobler, U., Experimental servicing satellite: Rendezvous maneuver in GEO controlled by a ground–based Radar, *Draft Final Report, DASA Jena–Optronik, Contract No. DJO/FGAN–2510/94*, FGAN–FHP, Wachtberg 1995.